Implicit, partially linearized, electromagnetic particle simulation of plasma drift-wave turbulence

Bruce I. Cohen and Andris M. Dimits
Lawrence Livermore National Laboratory, University of California, Livermore, California 94550
(Received 21 January 1997)

Implicit, perturbative algorithms [B. I. Cohen, A. M. Dimits, J. J. Stimson, and D. C. Barnes, Phys. Rev. E **53**, 2708 (1996)] are extended to address electromagnetic particle simulation of drift-wave instabilities in electron and ion plasmas with a strong applied magnetic field. The algorithms use gyrokinetic ions and drift-kinetic electrons with a realistic mass ratio. Implicit moment and direct implicit solutions of the coupled Maxwell and plasma dynamical equations are demonstrated. Aspects of the numerical dispersion properties are confirmed in test simulations. Applications to ion-temperature-gradient and collisionless drift instabilities in a two-dimensional slab with magnetic shear are presented that illustrate the efficacy of the algorithms and the electromagnetic effects. [S1063-651X(97)14208-8]

PACS number(s): 52.65.−y, 52.35.Qz, 02.70.−c

I. INTRODUCTION

This work extends previous research by combining and applying gyrokinetic [1], partially linearized [2,3] (i.e., perturbative), and implicit methods [4,5] to the study of drift-wave instabilities in magnetically confined plasmas with electromagnetic effects included. Drift-wave instabilities [6] produce anomalous losses of heat and particles in magnetic fusion experiments. The importance of drift-wave turbulence to tokamak performance is the motivation for the Numerical Tokamak Turbulence Project [7], a Grand Challenge Application in the High Performance Computing and Communications Program. The algorithm development and physics applications presented here contribute to this project.

The primary goal of this work is to construct an efficient algorithm to support the inclusion of electromagnetic coupling and kinetic electron physics into the particle simulations being used to study tokamak core turbulence [7]. We view this work as a stepping stone toward a more realistic simulation of fusion-relevant experiments. Turbulent transport in the core of tokamaks is dominated by drift-type instabilities that are predominantly electrostatic in character and in which toroidal geometry is important [6]. Of lesser importance in drift modes in current magnetic fusion experiments of interest are collisions and coupling of the electrostatic drift waves to shear-Alfvén waves (whose importance increases as the ratio of the plasma thermal pressure to the magnetic energy density increases), which have weak effects on the unstable drift modes. However, collisions and electromagnetic coupling are finite, and help to determine the marginal stability plasma conditions. Therefore, to make our simulation codes more realistic and relevant to current and future experiments, we have previously developed an efficient ion-ion collision algorithm [8] and implicit algorithms for kinetic electron effects [4,5], and introduce electromagnetic coupling here. In each case, we evaluate the properties of the algorithm and demonstrate its use in a simplified two-dimensional example with physics content that is both relevant to drift-type instabilities and is easy to understand. The primary thrust of these papers is algorithm development. Elsewhere we reported three-dimensional toroidal electrostatic simulation applications that are relevant to understanding core transport in current magnetic fusion experiments [9,10].

In this work we demonstrate the efficient simulation of drift-wave turbulence in a strongly magnetized plasma including electromagnetic effects. The turbulence is produced by instabilities in which both electron and ion kinetic effects can be important [6]. The appropriate orderings for drift-wave phenomena relevant to core confinement in tokamaks are that the mode frequency ω is much less than the ion cyclotron frequency Ω_i, $\omega \ll \Omega_i$, the wave number parallel to the unperturbed magnetic field $\mathbf{B}$ is much smaller than that perpendicular to $\mathbf{B}$, the product of the ion Larmor radius ρ_i and the perpendicular wave number $k_\perp$ satisfies $k_\perp \rho_i \leqslant O(1)$, the electron Larmor radius is much smaller than any of the lengths of interest, and the $\mathbf{E}\times\mathbf{B}$ drift velocity is much smaller than the thermal velocities. Our computational model is fitted to these orderings. As in previous work [5], we use gyrokinetic ion and drift-kinetic electrons in a partially linearized (δf) model. The quasineutral limit of Poisson's equation for the self-consistent electric potential and Ampere's law for the electromagnetic coupling of the drift waves to shear-Alfvén waves are solved for the self-consistent electromagnetic fields [11]. It is the inclusion of the coupling to shear-Alfvén waves, the introduction of the direct implicit method as an alternative to the implicit moment algorithm, and the examples including magnetic shear that distinguishes this work from that presented in Ref. [5]. Our use of implicit methods to reduce thermal noise carried by the shear-Alfvén waves and to ensure numerical stability, and our improved results with better spatial resolution in magnetically sheared simulations, differentiate this work from the thesis research of Cummings [12]. Our analysis and simulation experience with these implicit algorithms indicate that their stability is relatively robust, and they are both accurate and efficient.

The paper is organized as follows. In Sec. II we present outlines of both implicit moment and direct implicit electromagnetic algorithms. Test cases that illustrate some of their dispersion properties and applications to the ion-temperature-gradient (ITG) and collisionless drift instabilities including electromagnetic effects are reported in Sec. III. Conclusions are presented in Sec. IV. We find in the examples presented here and in Ref. [5] that δf and implicit-

ness are efficacious in reducing thermal noise. The implicit time-integration schemes ensure stability and relax certain constraints on the times step, but important accuracy constraints remain. The simulations succeed in resolving electromagnetic drift-wave phenomena with kinetic ions and electrons using a realistic mass ratio with relatively good efficiency.

II. IMPLICIT ELECTROMAGNETIC δf ALGORITHM

A. Model equations

The electromagnetic implicit δf algorithm in a magnetically sheared slab is characterized by the following inequalities and equations. The ions satisfy the reduced Vlasov-Maxwell equations [11,12] based on the following standard gyrokinetic orderings:

$$\frac{\delta f}{F_M}\sim\frac{q_i\phi}{T_i}\sim\frac{\delta B}{B}\sim\frac{\omega}{\Omega_i}\sim\frac{\rho_i}{L}\sim\epsilon\ll 1,\quad L\sim L_\parallel,$$

where $\rho_i\equiv v_i/\Omega_i$; $\Omega_i\equiv\epsilon B/m_i c$; $v_i\equiv\sqrt{T_i/m_i}$; q_i, m_i, and T_i, respectively, are the ion charge, mass, and temperature; c is the speed of light; B is the equilibrium magnetic-field strength; ϕ is the electrostatic potential; ω is the frequency of the perturbation; L is a characteristic perpendicular equilibrium scale length of the system; and $L_\parallel$ is the characteristic parallel wavelength of the perturbation.

In this ordering, the electric field is given by

$$\mathbf{E}=-\nabla\phi-\frac{1}{c}\frac{\partial A_z}{\partial t}\hat{\mathbf{z}}. \tag{1}$$

The partially linearized gyrokinetic Vlasov equation for a plasma with weak magnetic shear in slab geometry is [13,14]

$$\frac{\partial\delta f}{\partial t}+v_\parallel\hat{b}\cdot\frac{\partial\delta f}{\partial\mathbf{R}}-\frac{c}{B}\frac{\partial}{\partial\mathbf{R}}\cdot\left[\left(\frac{\partial\overline{\phi}}{\partial\mathbf{R}}\times\hat{\mathbf{b}}\right)\delta f\right]=\frac{qv_\parallel}{T}\overline{\mathbf{E}}\cdot\hat{\mathbf{b}}F_M-\kappa\frac{c}{B}\frac{\partial\overline{\phi}}{\partial y}F_M, \tag{2a}$$

where $\kappa\equiv-\nabla\ln F_M$, F_M is an equilibrium Maxwellian distribution function,

$$\overline{\phi}\equiv\frac{1}{2\pi}\int d\hat{\boldsymbol{\rho}}\,\phi(\mathbf{R}+\boldsymbol{\rho}), \tag{2b}$$

and analogously for $\overline{\mathbf{E}}$, $\mathbf{R}\equiv\mathbf{x}-\boldsymbol{\rho}$, $\boldsymbol{\rho}\equiv\mathbf{v}_\perp\times\hat{\mathbf{b}}/\Omega_i$, $\hat{\boldsymbol{\rho}}$ is a unit vector in the direction of $\boldsymbol{\rho}$, $\mathbf{x}$ is the particle position, $\mathbf{v}_\perp$ is the perpendicular velocity, $\delta f(\mathbf{R},\mu,v_\parallel,t)$ is the gyroaveraged perturbed distribution function, and $\mu\equiv v_\perp^2/2$. The electrostatic potential ϕ is given by the gyrokinetic Poisson equation which, for a single-ion species i, is

$$\nabla^2\phi-\frac{\tau(\phi-\widetilde{\phi})}{\lambda_D^2}=-4\pi e(\overline{n_i}-n_e), \tag{2c}$$

where

$$\widetilde{\phi}(\mathbf{x})\equiv\frac{1}{2\pi}\int d\mu\,d\hat{\boldsymbol{\rho}}\,\overline{\phi}(\mathbf{x}-\boldsymbol{\rho}), \tag{2d}$$

$$\overline{n(\mathbf{x})}\equiv\int d\mu\,dv_\parallel\,d\hat{\boldsymbol{\rho}}\,\delta f(\mathbf{x}-\boldsymbol{\rho},\mu,v_\parallel,t), \tag{2e}$$

and where $\tau\equiv T_e/T_i$, $\rho_s\equiv c_s/\Omega_i$, $c_s\equiv\sqrt{T_e/m_i}$, $k_\perp$ is the perpendicular wave number, $\lambda_D\equiv\sqrt{T_e/4\pi n_0 e^2}$ is the electron Debye length, and n_0 is the background ion number density. The angle integrations in Eqs. (2b) and (2e) are replaced by averages over four points on the Larmor orbit, combined with charge-deposition and field-interpolation calculations involving spatial weighting functions [1].

Ampere's law determines the parallel vector potential

$$-\nabla_\perp^2 A_z=\frac{4\pi}{c}(j_{e\parallel}+j_{i\parallel})\approx\frac{4\pi}{c}j_{e\parallel} \tag{3}$$

in this ordering. The parallel ion current is smaller than the electron current by $O(m_e/m_i)$ and is neglected. The parallel electron current is computed from the electron distribution function expressed in terms of the parallel canonical momentum per unit mass $p_{e\parallel}=v_{e\parallel}-eA_z/m_e c$,

$$j_{e\parallel}=\int d\mu\,dp_{e\parallel}(p_{e\parallel}+eA_z/m_e c)\,\delta f_e(\mathbf{x},\mu,p_z,t). \tag{4}$$

The term on the right side of Eq. (2a) containing κ represents the radial $\mathbf{E}\times\mathbf{B}$ advection from an equilibrium with gradients in the radial direction. In the presence of density and temperature gradients, for example, $\kappa=\kappa_n\{1+\eta(v^2/2v_i^2-3/2)\}$, where $\eta\equiv(d\ln T_0/d\ln n_0)$, and κ_n represents the density gradient. Here $\partial/\partial x$ represents a derivative in the direction of the equilibrium gradients, and $\partial/\partial y$ represents a derivative in the direction perpendicular to the unperturbed magnetic field and the equilibrium gradients. In slab geometry, the unperturbed magnetic field has its principal component in the z direction with amplitude B_0, and has a small component in the y direction. With no shear $B_y=$const, and with shear $B_y=B_0(x-x_0)/L_s$, where L_s is the magnetic shear length.

The partial linearization or δf approximation denotes the fact that there is no parallel acceleration nonlinearity in Eq. (2a). This fact is used in the partially linearized particle simulation method by recognizing that the characteristics of Eq. (2a) preserve any spatially uniform particle distribution. In addition, we employ a linearized multiscale method so that the effects of density and temperature nonuniformity appear only through κ on the right side of Eq. (2a), and similarly for the electrons. The $k_x=0$ components of ϕ are suppressed. A particle method is then introduced to solve Eq. (2a):

$$\delta f=\sum_j w_j(t)\,\delta(\mathbf{R}-\mathbf{R}_j)\,\delta(v_\parallel-v_{\parallel j})\,\delta(\mu-\mu_j), \tag{5}$$

where $\mathbf{R}_j$ and $v_{\parallel j}$ evolve according to the characteristic equations of Eq. (2a). In the absence of collisions, if the simulation particles j are loaded as a uniform Maxwellian then the source terms on the right side of Eq. (2a) are correctly taken into account if w_j evolves according to

$$\dot{w}_j=\frac{qv_\parallel}{T}\overline{\mathbf{E}}\cdot\hat{\mathbf{b}}-\kappa_i\frac{c}{B}\frac{\partial\overline{\phi}}{\partial y}$$

along the characteristics for the ions, and

$$\dot{w}_j=\frac{\dot{p}_{\|e}v_\|}{v_e^2}-\kappa_e\frac{c}{B}\frac{\partial\overline{\phi}}{\partial y}$$

for the electrons, where $\dot{p}_{\|e}=(e/m_e)\nabla_\|^{(0)}\phi-(e/m_e)v_\|\nabla_\|^{(0)}A_z/c$. In our implementation, a second-order-accurate predictor-corrector time integration of the ion equations of motion is used with a time step Δt_i. A four-point gyroaveraged ion charge deposition is computed on both predictor and corrector steps.

The electrons satisfy a drift-kinetic Vlasov equation that can be obtained from Eqs. (2a) and (5) by replacing ion quantities with electron quantities and taking the limit of the zero electron Larmor radius. No gyroaveraging is required in computing forces on the electrons (computed at the electron gyrocenter) nor in depositing their charge density or any other moment on the spatial grid.

The electron particle motion is calculated basically using the same predictor-corrector algorithm as the ions, but with a time step Δt_e that is a submultiple of the ion time step [15]. This is motivated by the fact that with a realistic ion-to-electron mass ratio, the parallel electron transit motion is typically much faster than that of the ions ($v_e\gg\nu_i$, where $v_e\equiv\sqrt{T_e/m_e}$ and $\nu_i\equiv\sqrt{T_i/m_i}$). A sequence of electron advances is calculated over a number of electron time steps adding up to the ion time step. The self-consistent electric field is updated on the ion time step.

B. Implicit moment equations

The solution of the Poisson equation, Eq. (2c), is rendered implicit, as described in Ref. [5] with the use of implicit moment equations for the electrons [16–18]. Use of implicit and δf methods removes undesirable high-frequency modes, reduces the thermal noise associated with these high-frequency modes, and ensures numerical stability [5]. The implicit moment equations are computed from the partially linearized drift-kinetic Vlasov equation:

$$\frac{\partial\delta f_e}{\partial t}+v_\|\hat{\mathbf{b}}\cdot\nabla\delta f_e+v_{\mathbf{E}\times\mathbf{B}}\cdot\nabla\delta f_e+\frac{ev_\|}{m_ev_e^2}F_{Me}\hat{\mathbf{b}}\cdot\mathbf{E}+\frac{c}{B}\frac{\partial\phi}{\partial y}\frac{F_{Me}}{L_{Te}}\left(\frac{L_{Te}}{L_{ne}}+\frac{v_\|^2}{2v_e^2}-\frac{1}{2}\right)=0. \tag{6}$$

Note that Eq. (6) can just as easily be written in terms of $p_\|$ instead of $v_\|$, and the unperturbed electron distribution function is also a Maxwellian in terms of the parallel canonical momentum. In finite-difference form for the time derivatives, the moment equations for the *perturbed* electron moments derived from Eq. (6) are

$$\frac{n_e^{n+1}-n_e^n}{\Delta t_i}+\nabla_\|[\epsilon_1 j_{e\|}^{n+1}+(1-\epsilon_1)j_{e\|}^n]=-\frac{n_0ev_{*e}}{T_e}\frac{\partial}{\partial y}[\epsilon_1\phi^{**}+(1-\epsilon_1)\phi^n]-(\mathbf{v}_{\mathbf{E}\times\mathbf{B}}\cdot\nabla_\perp n_e)^{**}, \tag{7}$$

$$\frac{j_{e\|}^{n+1}-j_{e\|}^n}{\Delta t_i}+v_e^2\nabla_\|[\epsilon_2 n_e^{n+1}+(1-\epsilon_2)n_e^n]+\nu_{\mathrm{ei}}[\epsilon_2 j_{e\|}^{n+1}+(1-\epsilon_2)j_{e\|}^n]-\frac{en_0}{m_e}\nabla_\|[\epsilon_2\phi^{n+1}+(1-\epsilon_2)\phi^n]-\frac{en_0}{m_ec}\frac{A_z^{n+1}-A_z^n}{\Delta t_i}=[-\mathbf{v}_{\mathbf{E}\times\mathbf{B}}\cdot\nabla_\perp j_{e\|}+\nu_{\mathrm{ei}}\overline{j_{i\|}}-\nabla_\|(P_{e\|}^{n+1/2}-n_ev_e^2)]^{**}, \tag{8}$$

where n_e is the electron number density; $j_{e\|}$ is the electron parallel current density per unit charge, i.e., the parallel flux density; $\mathbf{v}_{\mathbf{E}\times\mathbf{B}}$ is the $\mathbf{E}\times\mathbf{B}$ velocity at the electron gyrocenter; $v_{*e}\equiv(\rho_e/L_{ne})v_e$; ν_{ei} is the electron-ion collision rate; $P_{e\|}\equiv\langle v_{e\|}^2\rangle$ is the parallel pressure moment computed on the electron velocity distribution function; $j_{e\|}$ is the electron parallel flux density; $\overline{j_{i\|}}$ is the corresponding gyroaveraged ion parallel flux density that must be computed if $\nu_{\mathrm{ei}}\neq0$; and ϵ_1, ϵ_2, and ϵ_3 are centering parameters ($0\leqslant\epsilon_i\leqslant1$). The superscripts indicate electron time levels with the ** denoting time level n on the predictor pass and the predicted value at time level $n+1$ on the corrector pass in advancing quantities from time $n\Delta t_i$ to time $(n+1)\Delta t_i$. It is sufficient for controlling the linear dispersion to use $\nabla_\|=\hat{b}^{(0)}\cdot\nabla$ in the implicit moment equations.

Ampere's law is used to obtain A_z^{n+1} before solving Eqs. (7) and (8) for ϕ^{n+1}. A semi-implicit modification of Eq. (3) provides additional numerical dissipation,

$$\left[-\nabla_\perp^2+(1+\epsilon_2-\tfrac{1}{2})\frac{\omega_{\mathrm{pe}}^2}{c^2}\right]\frac{A_z^{n+1}}{c}=-\frac{\omega_{\mathrm{pe}}^2}{c^2}\left\langle\frac{p_{e\|}^{n+1}}{m_e}\right\rangle+(\epsilon_2-\tfrac{1}{2})\frac{\omega_{\mathrm{pe}}^2}{c^2}\frac{A_z^n}{c}, \tag{9}$$

where $\langle\ \rangle$ denotes the average over the electron velocity distribution function.

The moment equations are bound to the particle electrons by setting the number and flux densities, n_e^n and $j_{e\|}^n=n_e\langle p_{e\|}^n+eA_z^n/m_ec\rangle$ in Eqs. (7) and (8) equal to the corresponding particle moments accumulated on the spatial mesh. The electron parallel pressure moment is an orbit-averaged moment [19] computed from the simple average over the time interval $n\Delta t_i$ to $(n+1)\Delta t_i$ of the parallel electron pressure moment per unit mass accumulated at each Δt_e. The electron particle equations of motion are advanced in a predictor step from $n\Delta t_i$ to $(n+1)\Delta t_i$ using the electric and magnetic fields at $n\Delta t_i$ interpolated to the electron trajectories computed with Δt_e. The ions are advanced in one big predictor step from $n\Delta t_i$ to $(n+1)\Delta t_i$, and the gyroaveraged ion moments are computed before solving for the predicted fields at $(n+1)\Delta t_i$. On the corrector pass, the electrons are again advanced from $n\Delta t_i$ to $(n+1)\Delta t_i$, but $\phi^*=\epsilon_3\phi^{n+1}+(1-\epsilon_3)\phi^n$ is used to calculate forces and drifts. To have the electron fluid and particle motion synchronized as much as possible, we usually set $\epsilon_3=\epsilon_2$. The entire scheme is accurate to $O(\Delta t_i^2)$ if $\epsilon_1=\epsilon_2=\epsilon_3=\frac{1}{2}$.

Equations (7) and (8) are a linear system of equations for n_e^{n+1} and $j_{e\|}^{n+1}$ that is solved algebraically for n_e^{n+1}, which is then substituted into Eq. (2c) to determine ϕ^{n+1}. This ren-

ders the Poisson equation implicit because n_e^{n+1} depends linearly on ϕ^{n+1}. It is important to note that, in an electromagnetic model, both ϕ and A_z contribute to $E_\parallel$ in the equations of motion and on the right side of Eq. (8). Therefore, Ampere's equation, Eq. (9), is solved first to determine A_z before solving the implicit moment and Poisson equations to obtain ϕ.

The solution of the implicit gyrokinetic Poisson equation in a magnetically sheared domain was described in Ref. [5], but no simulation examples with magnetic shear were reported. For applications to tokamak core turbulence where $\omega_{\rm pi}^2/\Omega_i^2 \gg 1$, the vacuum polarization is negligible. Here, $\omega_{\rm pi}$ is the ion plasma frequency; and Ω_i is the ion cyclotron frequency. Poisson's equation becomes a statement of quasineutrality and takes the form

$$\left\{ \frac{\omega_{\rm pi}^2}{\Omega_i^2} \frac{[1-\Gamma_0(b)]}{\rho_i^2} + C\omega_{\rm pe}^2 \Delta t_i^2 k_\parallel^2(x) \right\} \phi(k_y,x)^{n+1} = S(k_y,x), \tag{10}$$

where $b=k_\perp^2\rho_i^2$, $\Gamma_0(b)=I_0(b)\exp(-b)$, I_0 is the modified Bessel function, $C \equiv \epsilon_1\epsilon_2/(1+\epsilon_1\epsilon_2 k_\parallel^2 v_e^2 \Delta t_i^2)$, and $k_\perp^2 = k_y^2 - \partial^2/\partial x^2$. The Poisson equation Eq. (10) can be conveniently solved with a Padé approximation $1-\Gamma_0(b) \approx b/(1+b)$, a Fourier transform in y, and finite differencing in x, leading to a tridiagonal matrix inversion. Simple periodic boundary conditions in x and y are used for simulations in an unsheared magnetic field with $B_y=$ const. For B_y a function of x, a bounded simulation model is used with $\phi=0$ at the boundaries in x; and periodic boundary conditions are used in y.

C. Direct implicit equations

A more compact implicit formulation is obtained by using a direct implicit algorithm [20–22]. The direct implicit gyrokinetic algorithm dispenses with the implicit moment equations altogether, and replaces the associated implicit Poisson equation with a slightly different implicit Poisson equation

$$\left\{ \frac{\omega_{\rm pi}^2}{\Omega_i^2} \frac{[1-\Gamma_0(b)]}{\rho_i^2} + c_0\omega_{\rm pe}^2 \Delta t_i^2 k_\parallel^2(x) \right\} \phi(k_y,x)^{n+1} = -c_1\omega_{\rm pe}^2 \Delta t_i^2 k_\parallel^2(x)\phi(k_y,x)^n + 4\pi e(\overline{n_i^{n+1}} - n_e^{n+1}) \tag{11}$$

in the quasineutral limit, where $k_\parallel$ is the parallel wave number computed in the unperturbed magnetic field, and c_0 and c_1 are constants that control stability and dissipation. As in the implicit moment algorithm, ion and electron charge densities are computed on the predictor step as an extrapolation of particle trajectories that do not yet depend on ϕ^{n+1} or A_z^{n+1}. On the corrector step, the particles are advanced in time using fields computed from ϕ^{n+1} or A_z^{n+1} as well as from field data from the previous time step, moments over the particle distributions are computed, and the field equations are solved again. In a traditional direct implicit algorithm, there would be another correction to the particle advance from time step n to $n+1$ using the corrected fields at time step $n+1$. This additional particle advance is omitted here, which contributes an additional factor to $O(\Delta t^2)$ errors. We note that in the direct implicit algorithm, there is no accumulation of the electron parallel stress $\langle P_{e\parallel} \rangle$. The rest of the direct implicit algorithm is the same as the implicit moment algorithm.

The second term on the left side of both Eqs. (10) and (11) controls the stability of the electrostatic shear Alfvén wave [1] at finite Δt_i and increases the dielectric shielding. The ratio of the second term to the first scales as $\omega_h^2 \Delta t_i^2 = k_\parallel^2 v_e^2 \Delta t_i^2 / k_\perp^2 \rho_s^2$. However, $\omega_h^2 \Delta t_i^2$ is limited somewhat by accuracy considerations, because $k_\parallel v_e \Delta t_i < 1$ to ensure the accuracy of the linear electron dielectric response and $k_\parallel/k_\perp \ll 1$ and $k_\perp \rho_s = O(1)$ to ensure the accuracy of the drift-type modes of interest. We will examine the dispersion properties of both implicit moment and direct implicit algorithms in the examples presented in Sec. III.

III. SIMULATION TEST CASES

In this section we present simulation examples of shear Alfvén waves, electromagnetic collisionless-drift and ion-temperature-gradient (ITG) instabilities in systems without magnetic shear, and electromagnetic ITG instability in systems with finite magnetic shear. These examples serve as tests of the algorithms, illustrate the basic dispersion and stability properties of the implicit algorithms, and elucidate some of the physics of kinetic electrons and electromagnetic effects on drift-type modes in a simple slab configuration.

A. Shear Alfvén waves

The highest-frequency normal mode supported by our physics model is the shear Alfvén wave [11,12,23]. In a cold uniform plasma the linear dispersion relation of the shear Alfvén wave is

$$\omega^2 = \frac{k_\parallel^2 v_A^2}{1 + \dfrac{k_\perp^2 c^2}{\omega_{\rm pe}^2}}, \tag{12}$$

where $v_A = (B_0^2/4\pi n_0 m_i)^{1/2}$ is the Alfvén velocity. For $k_\perp^2 c^2 \ll \omega_{\rm pe}^2$, $\omega^2 = k_\parallel^2 v_A^2$; and $\omega^2 = \omega_h^2 \equiv (k_\parallel^2/k_\perp^2)(m_i/m_e)\Omega_i^2$ for $k_\perp^2 c^2 \gg \omega_{\rm pe}^2$, which is the electrostatic limit. The generalization of Eq. (12) to a warm plasma is a straightforward [12]

$$\chi_{i\perp} + \frac{k_\parallel^2}{k_\perp^2}(\chi_{e\parallel} + \chi_{i\parallel}) \left(1 - \frac{\omega^2}{k_\parallel^2 c^2}\chi_{i\perp} \right) = 0, \tag{13}$$

where $\chi_{i\perp} = (\omega_{\rm pi}^2/\Omega_i^2)[1-\Gamma_0(b)]/b$, $b=k_\perp^2\rho_i^2$, $\Gamma_0(b) = I_0(b)\exp(-b)$, I_0 is the modified Bessel function, $\chi_{s\parallel} \equiv -(\omega_{ps}^2/2k_\parallel^2 v_s^2) Z'(\omega/\sqrt{2}k_\parallel v_s)$, $v_s \equiv (T_s/m_s)^{1/2}$, and Z' is the derivative of the plasma dispersion function.

In Ref. [5] we presented analyses of the numerical dispersion relation for the electrostatic limit of the shear Alfvén wave, and simulation results for cold and warm plasmas that agreed with simple theory. In Fig. 1 we show implicit moment simulation results for small-amplitude shear Alfvén waves with no magnetic shear and with $|\omega\Delta t_i| \ll 1$ in Fig. 1(a) and finite $|\omega\Delta t_i|$ in Fig. 1(b). In these simulations the implicit moment algorithm was used with a system $16\Delta x \times 16\Delta y$, 100 particles per cell for both electrons and

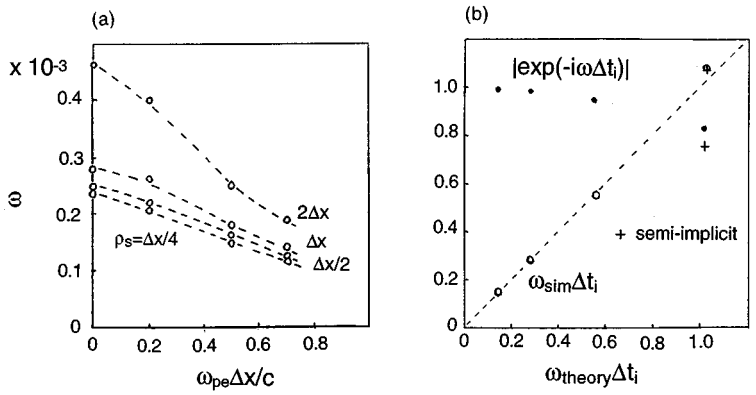

FIG. 1. The dispersion relation for a cold-plasma shear Alfvén wave and test simulation results with $\Delta t_i/\Delta t_e=5$. (a) Frequency ω vs $\omega_{pe}\Delta x/c$ for $0.5\leqslant\epsilon_1=\epsilon_2=\epsilon_3\leqslant 0.55$. (b) $\mathrm{Re}\omega\Delta t_i$ and the amplification factor $|\lambda|\equiv|\exp(-i\omega\Delta t_i)|$ vs $\omega_{\mathrm{theory}}\Delta t_i$ for $\omega_{pe}\Delta x/c=0.75$, $\beta m_i/m_e=0.5625$, and $\epsilon_1=\epsilon_2=\epsilon_3=0.55$. The dashed curves indicate analytical theory. Note that $\beta m_i/m_e=\omega_{pe}^2\rho_s^2/c^2$.

ions, $\Delta t_i/\Delta t_e=5$, uniform plasma, $B_y/B_0=0.01$, and $m_i/m_e=1836$. The results agree well with linear theory incorporating finite Δt effects. As $\omega\Delta t_i$ increases, the numerical damping of the shear Alfvén wave increases [the amplification factor $\lambda\equiv|\exp(-i\omega\Delta t_i)|$ decreases]. In Ref. [5] we performed a set of four simulations examining the Landau damping of electrostatic shear Alfvén waves. An example of Landau damping in an electromagnetic shear Alfvén wave is now given. With $\beta=(m_e/m_i)\rho_s^2\omega_{pe}^2/c^2$, $\rho_s=(T_e/m_i)^{1/2}/\Omega_i$, $\beta m_i/m_e=0.25$, $\rho_s/\Delta x=1$, $T_e=T_i$, $B_y/B_0=0.01$, $\omega_{pe}\Delta x/c=0.5$, $\omega_{pe}\Delta t_i=1000$, $k_y\rho_s=0.39$, $k_\parallel v_e\Delta t_i=0.18$, and $\omega_h\Delta t_i=0.23$, finite Δt effects and ion Landau damping were negligible. The solution of Eq. (13) gave $\mathrm{Re}\omega\Delta t_i=0.19$ and $\mathrm{Im}\omega\Delta t_i=-0.023$ due to electron Landau damping, while in the simulations we observed $\mathrm{Re}\omega\Delta t_i=0.18$ and $\mathrm{Im}\omega\Delta t_i=-0.02$. This good degree of agreement was similar to the electrostatic results in Ref. [5].

A mature literature exists on the dispersion properties of the direct implicit algorithm [21,22]. With $\epsilon_2=\frac{1}{2}$ in Eq. (9) to suppress the semi-implicit modification of Ampere's law, the direct implicit algorithm's dispersion relation for cold-plasma shear Alfvén waves is modeled by

$$\frac{1}{k_\parallel^2 v_A^2\Delta t_i^2}+\frac{1}{\omega_h^2\Delta t_i^2}+c_0+\frac{c_1}{\lambda}+\frac{\lambda}{(\lambda-1)^2}=0 \qquad (14)$$

in the limit $\Delta x\to 0$, where $\lambda\equiv\exp(-i\omega\Delta t_i)$. The last term on the left side of Eq. (14) is derived for a leap-frog time integration of the particle equations of motion, and is a useful model for the actual predictor-corrector scheme in our algorithm. For stability [21], $c_0+1/\omega_h^2\Delta t_i^2+1/k_\parallel^2 v_A\Delta t_i^2\geqslant 1/4$ and $c_1\geqslant 0$. There is finite dissipation for $c_1>0$. Guided by previous analysis and experience [21], we set $c_0=0.3$ and $0\leqslant c_1\leqslant 0.02$. Results for $\beta=0$ and 0.001 from direct implicit simulations with $\rho_s/\Delta x=0.5$, $T_e=T_i$, $B_y/B_0=0.01$, system size $16\Delta x\times 16\Delta y$, 100 particles per cell of each species, $m_i/m_e=1836$, and uniform plasma are plotted in Fig. 2.

Both implicit moment and direct implicit algorithms reproduce the linear dispersion relation of shear Alfvén waves to good accuracy including electron Landau damping. There is significant numerical dispersion and damping for $|\omega\Delta t_i|\geqslant 1$. In the earlier work of Reynders [23], in which the parallel electron current was computed directly from the parallel electron velocity, it was observed that shear Alfvén thermal noise grew steadily in simulations with a δf algorithm and $\beta m_i/m_e=O(1)$. As in Cummings' electromagnetic δf simulations that used the parallel electron canonical momentum from which to compute the parallel current [12], we did *not* see a steady growth of Alfvén wave noise.

B. Collisionless drift instability

Inverse electron Landau damping and a density gradient lead to the collisionless drift instability in an unsheared configuration [6,24]. Finite-β effects can significantly reduce linear growth rates for $\beta m_i/m_e=O(1)$. Here we report two-dimensional unsheared simulations of the collisionless drift instability with implicit moment and direct implicit algorithms, which illustrate electromagnetic effects. Implicit moment electrostatic simulations of collisionless drift instabilities were presented in Ref. [5].

Figures 3, 4, and 5 show results from implicit moment δf simulations with $T_e/T_i=4$, $\rho_s/L_n=0.214$, $m_i/m_e=1837$, $\Omega_e/\omega_{pe}=10$, $\lambda_e/\Delta x=1$, $\rho_s/\Delta x=4$, $B_y/B_0=0.01$, $32\Delta x\times 32\Delta y$, $\omega_{pe}\Delta t_i=200$, and $\Delta x=\Delta y$. The reference results in Fig. 3 were obtained with the implicit moment algorithm and $\beta=0$ [5]. The direct implicit simulation results for this case were essentially the same. Figures 4 and 5 show results for $\beta m_i/m_e=4$ obtained with the implicit moment and direct implicit algorithms, respectively, and with radial modes included ($k_x\neq 0$ and $k_y=0$). With $\beta m_i/m_e=4$, linear theory [12] predicts a 30–40 % reduction of the linear growth rate and a 10–20 % decrease in $|\mathrm{Re}\omega|$ for the $(k_x,k_y)=(1,-1)$ mode, where $k_y\rho_s=\pi/4$ in this unsheared system, relative to the $\beta=0$ case [1] for which $\omega/\Omega_i=-0.06+i0.011$. The simulation results in Figs. 4 and 5 are in

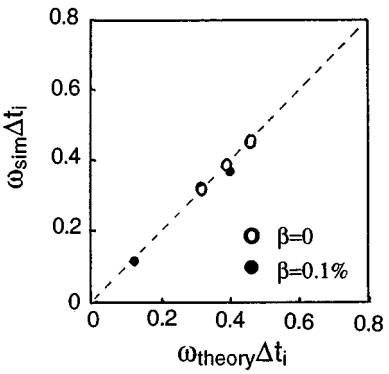

FIG. 2. The dispersion relation for a warm-plasma shear Alfvén wave and direct implicit simulation results for the observed $\mathrm{Re}\omega/\omega_h$ vs the theoretical prediction in a homogeneous, shear-free plasma for $\beta=0$ (○) and 0.001 (●).

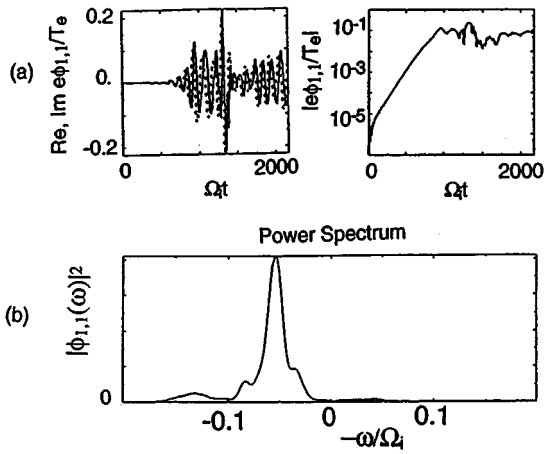

FIG. 3. Collisionless drift instability in a $32\Delta x \times 32\Delta y$ system with $\beta=0$ and no shear using the implicit moment algorithm (with $\epsilon_1=\epsilon_2=0.51$). (a) Re, Im, and absolute value of $e\phi_{1,1}/T_e$ vs $\Omega_i t$. (b) Power spectrum for the $(1,-1)$ mode.

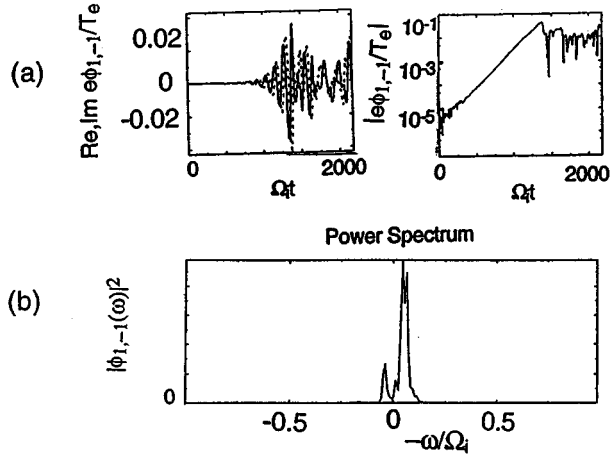

FIG. 5. Collisionless drift instability in a $32\Delta x \times 32\Delta y$ system with $\beta m_i/m_e=4$, no shear, and radial modes using the direct implicit moment algorithm (with $c_0=0.3$, $c_1=0.02$). (a) Re, Im, and absolute value of $e\phi_{1,1}/T_e$ vs $\Omega_i t$. (b) Power spectrum for the (1, -1) mode.

fairly good agreement with one another and with theory. The shear Alfvén waves were heavily damped by electrons here. Although the detailed nonlinear behavior differs somewhat, the linear behavior and the average nonlinear behavior are the same in Figs. 4 and 5. Because the post-saturation behavior was somewhat chaotic, differences in the algorithms and the initializations led to observable differences in the detailed time histories of the modes. The presence of radial modes in the simulations whose results are shown in Figs. 4 and 5 allowed the unstable drift waves to saturate at a significantly lower amplitude because of velocity shear effects associated with the radial modes. We return to a discussion of the importance of the radial modes later in the paper.

C. Ion-temperature-gradient instability in an unsheared slab

We also extended simulations of ITG instability with drift-kinetic electrons reported in Ref. [5] to finite β, and compared the results of implicit moment and direct implicit algorithms. A convenient ITG test case in an unsheared system was that introduced by Lee and Tang [25]. In Fig. 6 we show results of ITG simulations in a shearless slab using the implicit moment and direct implicit algorithms for $\beta=0$. The simulation parameters were $L_n/L_T=4$ for each species, $T_i=T_e$, $\rho_i/L_n=0.05$, $16\Delta x\times 16\Delta y$, $\Delta x=\Delta y=\rho_i$, $B_y/B_0=0.01$, $\epsilon_1=\epsilon_2=\epsilon_3=0.65$, $\omega_h\Delta t_i=0.933$, $\exp(-k^4a^4)$ smoothing with $a=0.9$, $\omega_{pe}\Delta t_i=4000$, $m_i/m_e=1836$, $\Omega_e/\omega_{pe}=1$, $n_0=64/\Delta x^2$, and $\Delta t_i/\Delta t_e=5$. Modes with $k_y=0$ and $|k|>10\pi/16\Delta y$ were suppressed in the electric potential.

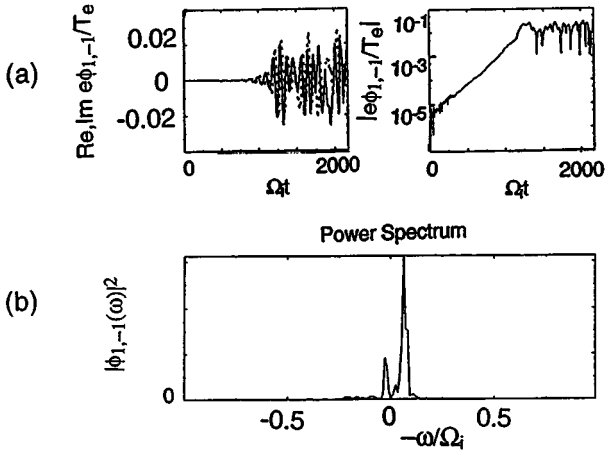

FIG. 4. Collisionless drift instability in a $32\Delta x \times 32\Delta y$ system with $\beta m_i/m_e=4$, no shear, and radial modes using the implicit moment algorithm (with $\epsilon_1=\epsilon_2=0.51$). (a) Re, Im, and the absolute value of $e\phi_{1,1}/T_e$ vs $\Omega_i t$. (b) Power spectrum for the (1, -1) mode.

In the implicit moment simulation $\epsilon_1=\epsilon_2=0.51$, and $c_0=0.3$ and $c_1=0.02$ in the direct implicit simulation. In the linear phase, the frequency and growth rate were $\omega/\Omega_i=-0.006+i0.0046$ in both simulations for the $(k_x,k_y)=(1,-1)$ mode, where $k_y\rho_s=\pi/8$, in very good agreement with theory, $\omega/\Omega_i=-0.006+i0.0046$ [25]. The nonlinear saturation is substantially the same, but the post-saturation chaotic behavior in the time histories of the modes differed in small details.

For $\beta m_i/m_e=2.25$ and other parameters the same, there is little stabilization expected [12], and only a 2–3% reduction in the linear growth rate was observed for the $(k_x,k_y)=(1,-1)$ mode shown in Fig. 7. There was negligible change in the cross-field ion thermal transport from the $\beta=0$ case. The results from the implicit moment and direct implicit simulations for the finite-β case agreed with one another quite well. These results concur with those reported by Cummings [12].

The two implicit algorithms are effective in suppressing ω_h noise in the electrostatic shear-free simulations of the collisionless drift instability (Fig. 3) and the ITG instability (Fig. 6). The implicit electromagnetic simulations of collisionless drift and ITG instabilities at finite β shown here are effective in suppressing Alfvén wave thermal noise. In using the implicit moment algorithm, good results were obtained for $0.51\leqslant\epsilon_{1,2}\leqslant 0.6$; and optimal results for the best signal-to-noise were obtained by adjusting $\epsilon_{1,2}$ to values that depended somewhat on the specific application. This is illustrated in Fig. 8, where we show a simulation result for ITG

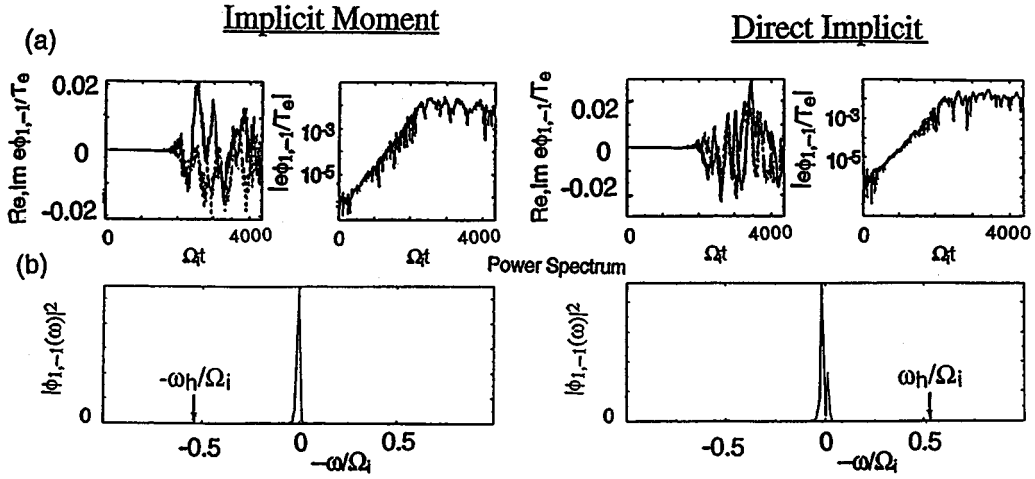

FIG. 6. Ion-temperature-gradient simulation results with drift-kinetic electrons using the implicit moment (with $\epsilon_1=\epsilon_2=0.51$) and direct implicit (with $c_0=0.3$, $c_1=0.02$) δf algorithms for $\beta=0$ and no shear. (a) Re, Im, and absolute value of $e\phi_{1,-1}/T_e$ vs $\Omega_i t$ and (b) corresponding power spectrum vs frequency.

instability (with $\beta m_i/m_e=2.25$ and $\epsilon_1=\epsilon_2=0.6$ in the implicit moment algorithm) that has a much higher level of shear Alfvén wave noise than does the simulation shown in Fig. 7 (with $\epsilon_1=\epsilon_2=0.51$ and other parameters the same).

D. Ion-temperature-gradient instability in a sheared magnetic field

In Ref. [5] we introduced an implicit moment algorithm for use in a sheared magnetic field, but reported only electrostatic simulations in unsheared systems. Here we present experience with implicit simulations in a magnetically sheared system.

Reynders [23,26] has studied the linear structure of an ITG instability in a sheared slab based on solutions of the linearized Vlasov-Maxwell equations using an integral equation solver [27]. Substantial stabilization is predicted for ITG in a sheared slab at $\beta=1\%$ with $\eta_i=2$, $\eta_e=0$, $L_s/L_n=40$, and $T_e=T_i$. However, both Reynders [23] and Cummings [12] observed very little linear stabilization due to finite β in their electromagnetic gyrokinetic δf simulations. In Fig. 9 we show results that concur with Reynders' and Cummings' earlier simulation results when we used parameters: $\rho_s=3\Delta x$, system size $128\Delta x\times 32\Delta y$, $\Delta t_i/\Delta t_e=4$, $c_0=0.3$, and $c_1=0.02$ (direct implicit algorithm), and with either 37 000 or 66 000 ions and electrons. When we increased β from 0 to 0.5%, we observed a reduction in the linear growth rate of the $k_y\rho_s=0.6$ mode of 10% instead of the 60% reduction predicted by linear theory [23]. Thus, with these simulation parameters, the simulations failed to observe the correct reduction in growth rates due to finite β.

Cummings [12] pointed out that the width of the narrow nonadiabatic electron layer Δx_e can be difficult to resolve. The width of the nonadiabatic electron layer is determined by $|\omega/k_\parallel v_e|\sim 1$, where $k_\parallel=k_y\Delta x_e/L_s$. For the example presented in Fig. 9, $\Delta x_e/\Delta x=0.2$, i.e., the electron layer is one-fifth of a grid cell wide. Furthermore, the narrowest feature in the ITG eigenfunction has width ρ_s, which is inadequately resolved by the grid when $\rho_s=3\Delta x$.

Simulation results that were in better agreement with theory were obtained with twice the spatial resolution. With

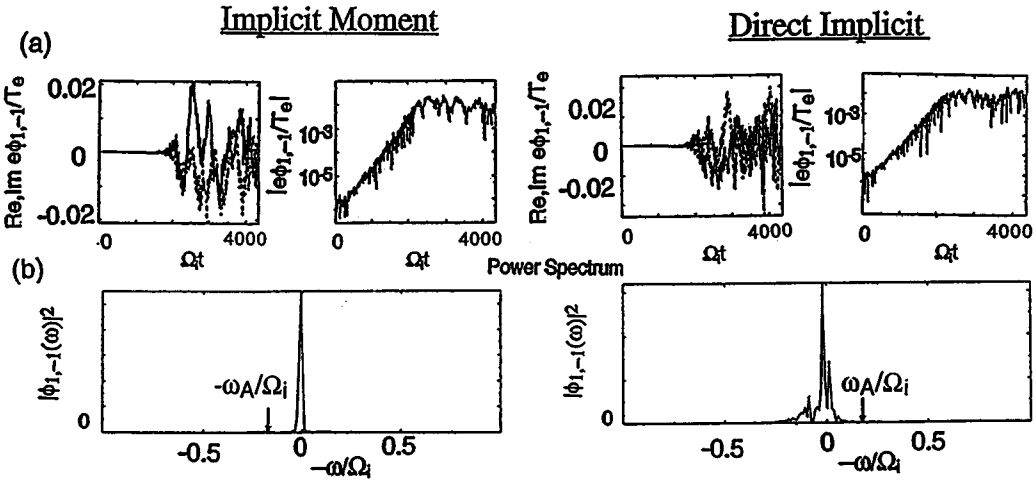

FIG. 7. Ion-temperature-gradient simulation results with drift-kinetic electrons using the implicit moment (with $\epsilon_1=\epsilon_2=0.51$) and direct implicit (with $c_0=0.3$, $c_1=0.02$) δf algorithms for $\beta m_i/m_e=2.25$ and no shear. (a) Re, Im, and absolute value of $e\phi_{1,-1}/T_e$ vs $\Omega_i t$ and (b) corresponding power spectrum vs frequency.

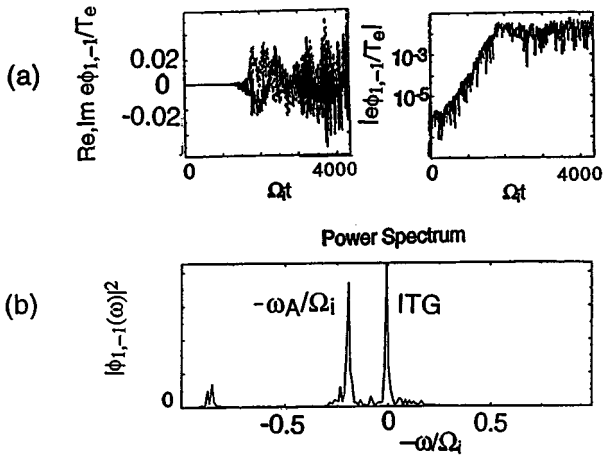

FIG. 8. Ion-temperature-gradient simulation results with drift-kinetic electrons using the implicit moment δf algorithm (with $\epsilon_1 = \epsilon_2 = 0.6$) for $\beta m_i/m_e = 2.25$, and no shear. (a) Re, Im, and absolute value of $e\phi_{1,-1}/T_e$ vs $\Omega_i t$ and (b) corresponding power spectrum vs frequency.

$\rho_s = 6\Delta x$, $128\Delta x \times 64\Delta y$, 74-K ions and electrons, and other parameters as in Fig. 9, we obtained the simulation results shown in Fig. 10. The linear frequency and growth rate for the $k_y\rho_s = 0.6$ mode agreed well with theory and with the simulation results in Fig. 9 for $\beta = 0$, where the electron kinetics were unimportant. However, a 35% reduction in the linear growth rate for the $k_y\rho_s = 0.6$ was observed for $\beta \sim 0.1\%$ in the $\rho_s = 6\Delta x$ simulation. A 25% reduction in the growth rate and little change in the real part of the frequency were expected based on the linear theory. In this case, $\Delta x_e/\Delta x = 0.4$; and there was adequate resolution of the electron distribution within Δx_e. In addition, with $\rho_s = 6\Delta x$ there are six grid cells to resolve the smallest feature of the eigenfunction. This resolution was a significant improvement over $\rho_s = 3\Delta x$. We attributed the better agreement with linear theory at finite β in this case to the improved spatial resolution of both the eigenfunction and the electron layer. We also performed a simulation with $\rho_s = 6\Delta x$ and $\beta = 2\%$ for which the $k_y\rho_s = 0.6$ mode was expected to be stable. Over the same time interval as shown in Fig. 10, there was very little growth of the $k_y\rho_s = 0.6$ mode out of the noise background ($\mathrm{Im}\omega/\Omega_i < 0.005\rho_s/L_T$), and it was very difficult to identify an ITG mode in the power spectrum. Of course, an initial-value code is typically very poorly suited to exploring stability near marginal stability.

There were some additional physics observations of interest in these ITG simulations. In Fig. 10 in the contour plots of $e\phi/T_e$ and A_z as functions of x and y at the end of the simulation, we note that A_z and, hence, the perturbed parallel current have even symmetry with respect to the single-mode rational surface ($k_\parallel = 0$) at $x = 64$. In consequence, B_x also has even symmetry, which is the same symmetry as a microtearing mode [28].

Although the relative magnetic perturbation B_x/B_0 was smaller by two orders of magnitude than the magnitude of $e\phi/T_e$, the effect on the linear growth rate was significant when there was adequate spatial resolution. This in turn affected the cross-field ion thermal transport in an important way because of the phase sensitivity of the transport. For weak but finite β in the ordering of this model, the ITG ion thermal transport as described by a quasilinear development remains dominated by the $\mathbf{E}\times\mathbf{B}$ motion of the fluid elements whose energy density perturbation at first order in wave amplitude scales as $\nabla\cdot(n_0 T_i \mathbf{v}_{\mathbf{E}\times\mathbf{B}})/i\omega \sim \mathbf{v}_{\mathbf{E}\times\mathbf{B}}\cdot\nabla(n_0 T_i)/i\omega$ per mode, because $\nabla\cdot\mathbf{v}_{\mathbf{E}\times\mathbf{B}} \approx 0$. At second order, the time-averaged quasilinear ion thermal flux Q_x^i scales dominantly as $Q_x^i \sim -(\gamma/\omega^2)\kappa n_0 T_i (\mathbf{v}_{\mathbf{E}\times\mathbf{B}}\cdot\hat{\mathbf{x}})^2$ per mode, where $\gamma \equiv \mathrm{Im}\omega$ and $\kappa \equiv \nabla_x \ln(n_0 T_i)$, i.e., there is a quasilinear heat flux down the pressure gradient that depends on the mode growth rate. Thus the dominant effect of increasing β on the ion thermal flux Q_x^i expected on the basis of a quasilinear

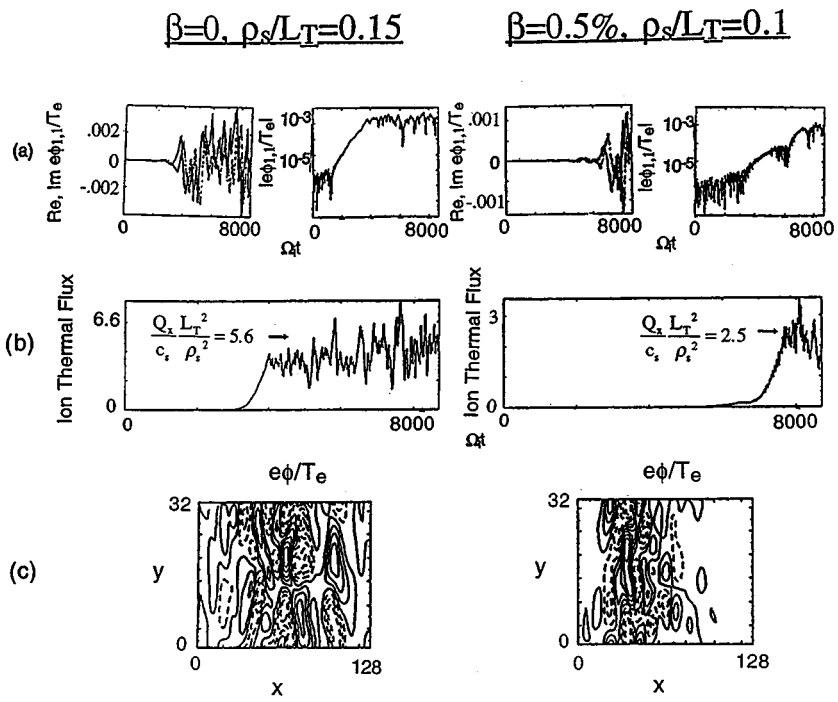

FIG. 9. Ion-temperature-gradient simulation results with drift-kinetic electrons using the direct implicit δf algorithm for $\beta = 0$ and $\beta = 0.5\%$, $L_s/L_n = 40$, $\eta_i = 2$ and $\eta_i = 0$, and with $\rho_s = 3\Delta x$. (a) Re, Im, and absolute value of $e\phi_{1,1}/T_e$ vs $\Omega_i t$, (b) ion thermal flux vs time, and (c) a contour plot of $e\phi(x,y)/T_e$ at the end of the simulation.

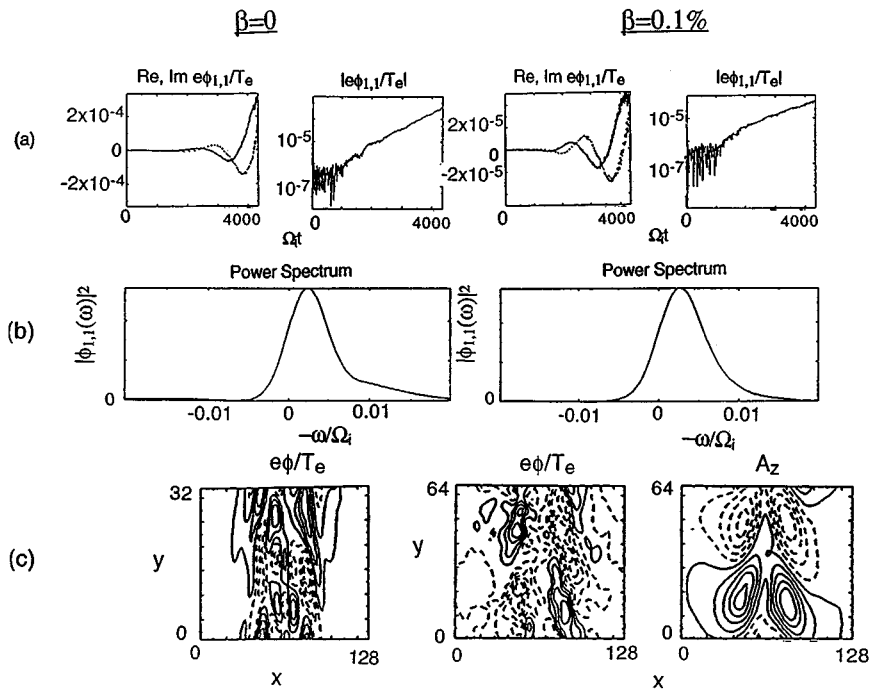

FIG. 10. Ion-temperature-gradient simulation results with drift-kinetic electrons using the direct implicit δf algorithm for $\beta=0$ and $\beta=0.1\%$, $L_s/L_n=40$, $\eta_i=2$ and $\eta_i=0$, and with $\rho_s=6\Delta x$. (a) Re, Im, and absolute value of $e\phi_{1,1}/T_e$ vs $\Omega_i t$. (b) Power spectrum in frequency for $\phi_{1,1}$. (c) Contour plot of $e\phi(x,y)/T_e$ and A_z at the end of the simulation.

argument is a reduction caused by linear stabilization. This conclusion agrees qualitatively with our simulations, all of which demonstrated a reduction in Q_x^i accompanying finite-β produced decreases in the linear growth rates.

A final physics observation concerns the influence of radial modes ($k_x\neq 0$ and $k_y=0$ in our two-dimensional system). When these modes were included in the simulations, they were driven to finite amplitude by the nonlinear action of the linearly unstable modes [9,29,30]. The radial modes produced a sheared $\mathbf{E}\times\mathbf{B}$ flow that sheared apart the turbulent eddies of the drift instabilities and reduced the transport. This has been well documented by theoretical arguments [30,31] and in simulations [12,29,32], and identified as an important factor in tokamak experiments [33]. In previous electrostatic simulations [5,29], the inclusion of radial modes led to steady states with large shear flows and reduced levels of turbulence and concomitant ion thermal transport in comparison to simulations with the radial modes suppressed. We observed that the same was true here in finite-β simulations in sheared and unsheared magnetic fields.

IV. CONCLUSIONS

In this paper we extended previous work that combined the implicit moment method with a partial linearization of the Vlasov-Poisson equations to incorporate the electromagnetic effects of coupling to shear Alfvén waves. We specialized to gyrokinetic ions and drift-kinetic, subcycled electrons, motivated by the time scales of interest in simulating core transport in tokamaks. We introduced an alternative, more compact implicit formulation using the direct implicit algorithm. In addition, we used an electromagnetic formulation in which the parallel electron current was computed from the parallel canonical momentum. Analysis and testing of the basic dispersion properties of the implicit algorithms confirmed successful implementations. We performed simulations of drift-type microinstabilities in a two-dimensional sheared slab configuration that illustrated both the usefulness of these algorithms and some of the physics of finite β and kinetic electrons.

The use of implicitness and partial linearization are effective in reducing thermal noise, which in turn allows the use of fewer particles to achieve acceptable results. Implicitness also makes the stability of the algorithms more robust. However, important accuracy constraints remain: $\omega\Delta t<1$, $k_\parallel v\Delta t<1$, $k_\perp v_{\mathbf{E}\times\mathbf{B}}\Delta t<1$, $k_\perp\Delta x_\perp<1$, $k_\parallel\Delta x_\parallel<1$, $\omega_{pe}\Delta x/c<1$, and $\rho_s/\Delta x\geq 1$. With magnetic shear, there are additional restrictions on spatial and statistical resolution due to the nonadiabatic electron layer surrounding the mode rational surface. We note that in an analogous finite-β gyrofluid algorithm, there would have to be many grid cells within the electron layer, while in the particle code there must be many cells per ρ_s (a less severe constraint), and there must be adequate statistics to resolve the electron distribution and its response within the layer.

We are pleased with the efficiency of these algorithms. For ITG simulations in an unsheared magnetic field (results shown in Figs. 6 and 7, and in Ref. [5]), electrostatic simulations with adiabatic electrons required $\sim 8\ \mu s/\Delta t_i$ per particle ion on the Cray C-90. Implicit moment electrostatic simulations with kinetic electrons, $m_i/m_e=1836$, equal numbers of ions and electrons, and $\Delta t_i/\Delta t_e=5$ required $\sim 20\ \mu s/\Delta t_i$ per ion, while implicit moment electromagnetic simulations required $\sim 30\ \mu s/\Delta t_i$ per ion and direct implicit electromagnetic simulations were slightly faster at $\sim 26\ \mu s/\Delta t_i$ per ion. The timings quoted here depend on the specific balance between particle pushing and field solving, and on the match of the computations to the natural length of the vector processors. For the ITG simulations reported here, the largest Δt_i (with $\Delta t_i/\Delta t_e=5$) that we used with drift-kinetic electrons included was one-half that of the Δt_i used with adiabatic electrons based on accuracy and convergence considerations. Thus the timings are dependent on the appli-

cation and the parameters. That the inclusion of drift-kinetic electrons with realistic mass ratio increased the computational costs by less than a factor of 8 in these examples, rather than by a factor like $(m_i/m_e)^{1/2}$, is very encouraging. A technique successfully used by W. W. Lee and co-workers to achieve additional economy in modeling electrons is to use a particle model only for the potentially resonant electrons and to represent the remaining, nonresonant electrons as an adiabatic fluid. This is especially attractive for higher β values in fusion-relevant plasmas because $v_e^2/v_A^2 = \beta m_i/m_e$, and the bulk of the electrons becomes increasingly adiabatic for $\beta m_i/m_e > 1$.

ACKNOWLEDGMENTS

We are grateful to W. Lee, S. Parker, J. Reynders, and J. Cummings for useful discussions and suggestions. This work was performed for the U.S. Department of Energy under Contract No. W-7405-ENG-48 at the Lawrence Livermore National Laboratory, and contributes to the Numerical Tokamak Turbulence Project, which is an activity supported jointly by the U.S. Department of Energy's Office of Fusion Energy Sciences and the Mathematics, Information, and Computational Sciences Division as part of the High Performance Computing and Communications Program.

[1] W. W. Lee, J. Comput. Phys. **72**, 243 (1987).
[2] M. Kotschenreuther, Bull. Am. Phys. Soc. **34**, 2107 (1988); (private communication); and (unpublished); R. E. Denton and M. Kotschenreuther, J. Comput. Phys. **119**, 283 (1995).
[3] A. M. Dimits and W. W. Lee, J. Comput. Phys. **107**, 309 (1993).
[4] B. I. Cohen and T. J. Williams, J. Comput. Phys. **107**, 282 (1993).
[5] B. I. Cohen, A. M. Dimits, J. J. Stimson, and D. C. Barnes, Phys. Rev. E **53**, 2708 (1996).
[6] W. M. Tang, Nucl. Fusion **18**, 1089 (1978).
[7] B. I. Cohen, D. C. Barnes, J. M. Dawson, G. W. Hammett, W. W. Lee, G. D. Kerbel, J.-N. Leboeuf, P. C. Liewer, T. Tajima, and R. E. Waltz, Comput. Phys. Commun. **87**, 1 (1995).
[8] A. M. Dimits and B. I. Cohen, Phys. Rev. E **49**, 709 (1994).
[9] A. M. Dimits, J. A. Byers, T. J. Williams, B. I. Cohen, X. Q. Xu, R. H. Cohen, J. A. Crotinger, and A. I. Shestakov, in *Fifteenth International Conference on Plasma Physics and Controlled Nuclear Fusion Research 1994*, Seville, Spain, 1994, IAEA-CN-60/D-P5 (IAEA, Vienna, 1995), Vol. 3, p. 457.
[10] A. M. Dimits, T. J. Williams, J. A. Byers, and B. I. Cohen, Phys. Rev. Lett. **77**, 71 (1996).
[11] T. S. Hahm, W. W. Lee, and A. Brizard, Phys. Fluids **31**, 1940 (1988).
[12] J. C. Cummings, Ph.D. thesis, Princeton University, 1995.
[13] E. A. Frieman and Liu Chen, Phys. Fluids **25**, 502 (1982).
[14] W. W. Lee, Phys. Fluids **26**, 556 (1983).
[15] J. C. Adam, A. Gourdin-Serveniere, and A. B. Langdon, J. Comput. Phys. **47**, 229 (1982).
[16] J. Denavit, J. Comput. Phys. **42**, 337 (1981).
[17] R. J. Mason, Phys. Fluids **23**, 2204 (1980); J. Comput. Phys. **41**, 233 (1981); Phys. Rev. Lett. **47**, 652 (1981).
[18] J. U. Brackbill and D. W. Forslund, in *Multiple Time Scales*, edited by J. U. Brackbill and B. I. Cohen (Academic, Orlando, 1985), Chap. 9.
[19] B. I. Cohen, in *Multiple Time Scales* (Ref. [18]), Chap. 10.
[20] A. Friedman, A. B. Langdon, and B. I. Cohen, Comments Plasma Phys. Control. Fusion **6**, 225 (1981).
[21] B. I. Cohen, A. B. Langdon, and A. Friedman, J. Comput. Phys. **46**, 15 (1982).
[22] A. B. Langdon, A. Friedman, and B. I. Cohen, J. Comput. Phys. **51**, 107 (1983).
[23] J. V. W. Reynders, Ph.D. thesis, Princeton University, 1992.
[24] W. W. Lee, J. H. Krommes, C. R. Oberman, and R. A. Smith, Phys. Fluids **27**, 2652 (1984).
[25] W. W. Lee and W. M. Tang, Phys. Fluids **31**, 612 (1988).
[26] J. V. W. Reynders, Phys. Plasmas **1**, 1953 (1994).
[27] R. Linsker, Phys. Fluids **24**, 1485 (1981).
[28] J. Wesson, *Tokamaks* (Clarendon, Oxford, 1987), p. 198.
[29] B. I. Cohen, T. J. Williams, A. M. Dimits, and J. A. Byers, Phys. Fluids B **5**, 2967 (1993).
[30] H. Biglari, P. H. Diamond, and P. W. Terry, Phys. Fluids B **2**, 1 (1990); Y. B. Kim, P. H. Diamond, and R. J. Groebner, *ibid.* **3**, 2050 (1991).
[31] A. Hassam, T. M. Antonsen, Jr., J. F. Drake, and C. S. Liu, Phys. Rev. Lett. **66**, 309 (1991).
[32] R. E. Waltz, G. D. Kerbel, and J. Milovich, Phys. Plasmas **1**, 2229 (1994); R. E. Waltz, G. D. Kerbel, J. Milovich, and G. W. Hammett, *ibid.* **2**, 2408 (1995).
[33] S. J. Zweben, Phys. Fluids **28**, 974 (1985); R. J. Groebner, K. H. Burrell, and R. P. Seraydarian, Phys. Rev. Lett. **64**, 3015 (1990); K. Ida, S. Hidekuma, Y. Miura, T. Fujita, M. Moir, K. Hoshino, N. Suzuki, and T. Yamauchi, *ibid.* **65**, 1364 (1990).